Check for updates

small methods
www.small-methods.com

Dual-Use Self-Assembled Monolayer Controlling Charge Carrier Extraction in Organic Solar Cells

Zhuo Xu, Rico Meitzner, Aman Anand, Aurelien Sokeng Djoumessi, Steffi Stumpf, Christof Neumann, Andrey Turchanin, Frank A. Müller, Ulrich S. Schubert, and Harald Hoppe**

The development and use of interface materials are essential to the continued advancement of organic solar cells (OSCs) performance. Self-assembled monolayer (SAM) materials have drawn attention because of their simple structure and affordable price. Due to their unique properties, they may be used in inverted devices as a modification layer for modifying ZnO or as a hole transport layer (HTL) in place of typical poly(3,4-ethylenedioxythiophene)-poly(styrenesulfonate) (PEDOT:PSS) in conventional devices. In this work, zinc oxide (ZnO) is modified using five structurally similar SAM materials. This resulted in a smoother surface, a decrease in work function, a suppression of charge recombination, and an increase in device efficiency and photostability. In addition, they can introduced asfor hole extraction layer between the active layer and MoO_3, enabling the use of the same material at several functional layers in the same device. Through systematic orthogonal evaluation, it is shown that some SAM/active layer/SAM combinations still offered device efficiencies comparable to ZnO/SAM, but with improved device' photostability. This study may provide recommendations for future SAM material's design and development as well as a strategy for boosting device performance by using the same material across both sides of the photoactive layer in OSCs.

1. Introduction

Organic solar cells (OSCs), as third-generation devices, have attracted the attention of many researchers due to their lightweight, high power-to-weight ratio, and the advantage of large-area fabrication on flexible substrates.[1–7] Recently, the development of new organic photovoltaic materials, in particular non-fullerene acceptor materials, has greatly improved the efficiency of OSCs, exceeding 19%.[8–11] The interface layer, one of the crucial parts in the design of OSCs, serves as an essential component for altering the electrode, blocking exciton losses, boosting selective charge extraction, lowering surface charge recombination, and promoting device efficiency and stability.[12–18]

In general, in OSCs, the electrode interfacial buffer layers can be divided into the cathode buffer layer, which is also known as the electron transport layer (ETL) or electron extraction layer,

Z. Xu, R. Meitzner, A. Anand, A. S. Djoumessi, S. Stumpf, U. S. Schubert, H. Hoppe
Laboratory of Organic and Macromolecular Chemistry (IOMC)
Friedrich Schiller University Jena
Humboldtstrasse 10, 07743 Jena, Germany
E-mail: zhuo.xu@uni-jena.de; harald.hoppe@uni-jena.de

Z. Xu, R. Meitzner, A. Anand, A. S. Djoumessi, C. Neumann, A. Turchanin, F. A. Müller, U. S. Schubert, H. Hoppe
Center for Energy and Environmental Chemistry Jena (CEEC Jena)
Friedrich Schiller University Jena
Philosophenweg 7a, 07743 Jena, Germany

R. Meitzner
Helmholtz-Zentrum Berlin GmbH
Hahn-Meitner Platz 1, 14109 Berlin, Germany

S. Stumpf, C. Neumann, A. Turchanin, F. A. Müller, U. S. Schubert
Jena Center for Soft Matter (JCSM)
Friedrich Schiller University Jena
Philosophenweg 7, 07743 Jena, Germany

C. Neumann, A. Turchanin
Institute of Physical Chemistry
Friedrich Schiller University Jena
Lessingstrasse 10, 07743 Jena, Germany

C. Neumann, A. Turchanin
Abbe Center of Photonics
Albert-Einstein-Strasse 6, 07745 Jena, Germany

F. A. Müller
Otto-Schott-Institute of Materials Research (OSIM)
Friedrich-Schiller-University of Jena
Löbdergraben 32, 07743 Jena, Germany

The ORCID identification number(s) for the author(s) of this article can be found under https://doi.org/10.1002/smtd.202301451

© 2023 The Authors. Small Methods published by Wiley-VCH GmbH. This is an open access article under the terms of the Creative Commons Attribution-NonCommercial-NoDerivs License, which permits use and distribution in any medium, provided the original work is properly cited, the use is non-commercial and no modifications or adaptations are made.

DOI: 10.1002/smtd.202301451

and the anode modification layer, which is also called the hole transport layer (HTL) or hole extraction layer. The anode modification layer mainly includes conductive polymers, such as poly(3,4-ethylenedioxythiophene)-poly(styrenesulfonate) (PEDOT:PSS)[19] and poly(ethylene imine) (PEI),[20] small molecules, like (*N*,*N*′-diphenyl)-*N*,*N*′- bis(1-naphthyl)−1,1′-biphenyl-4,4′-diamine[21] and self-assembled monolayer (SAM),[22] and metal oxides, such as molybdenum oxide (MoO_3),[23] vanadium oxide,[24] tungsten oxide,[25] etc. In the conventional device structure, the anode modification layer PEDOT:PSS has achieved great success in fundamental research and commercial applications due to its excellent solution processability and good conductivity.[26–30] However, its relatively poor transparency and slightly acidic nature, as well as its hygroscopicity, can lead to a decrease in device performance and stability.[31–37] As a consequence, people are more inclined to use small molecules or metal oxides as HTL in OSCs to improve device stability. Beaumont et al. achieved an enhanced performance from 1.3% to 3.3% compared to bare indium tin oxide (ITO) by using the SAM of chlorobenzoic acid and directly modifying ITO in the fabrication of conventional OSCs.[38] MoO_3 is widely used as an HTL and is often combined with zinc oxide (ZnO) ETL, yielding together the most common inverted device structure. The preparation process of ZnO involves casting its precursor at high temperatures to create a mesoporous film. Its unique structure and process operation results in a rough surface, which leads to poor ohmic contact with the active layer, thereby increasing the surface resistance in OSCs.[39–42] Additionally, the dangling —OH bonds on the surface or crystal surface and oxygen defects will trap charges, which induce trap-assisted charge recombination in OSCs and hamper the power conversion process.[43–45] Under light illumination, the light-induced free radicals in ZnO will attack receptor terminal groups through nucleophilic reactions, leading to the degradation of the conjugated structure of the photovoltaic material. This degradation causes a decrease in device performance and accelerates deterioration.[46,47] Interface modification methods are commonly employed to address the challenges posed by ZnO surface roughness and photocatalysis, which lead to decreased device efficiency and photostability.[48] These methods aim to reduce surface roughness and eliminate —OH groups on the ZnO surface. Examples of such methods include the use of polymer compounds, such as PEI and biomacromolecules,[49,50] fatty acids,[51] fullerene derivatives,[52] amino acids,[39] and SAM.[53–55] These modifiers deposit on the ZnO will repair surface defects and form a dipole at the ZnO interface, reducing the trap-assisted recombination at the interface and improves exciton extraction and transfer efficiency of OSCs. From this, it can be seen that the SAM material exhibits different functions due to its specific location in the device. It can be used to modify the surface of ZnO as the ETL part in inverted devices, or directly used as the HTL modification on ITO in traditional devices. Moreover, there are rare reports on the strategy of incorporating the same material at both sides of the active layer to fabricate single-junction OSCs.

Therefore, in this work, the structurally similar self-assembled small molecular materials were selected to modify ZnO for application in inverted OSCs based on the PM6:Y6 system. Try to use small molecule acids to optimize the surface of ZnO, reduce residual —OH groups, achieving in improved device performance and photostability. The optimized performance of the device is correlated with the pK_a of SAM materials, which provides practical guidance for selecting small molecule materials as modifying layers in inverted OSCs. The enhanced photostability of SAM certain devices can be attributed to their passivation of the photocatalytic activity of ZnO. However, some SAMs with lower binding affinity to electron lone pairs due to certain molecular structures result in lower device photostability compared to the unmodified ones. Interestingly, when the small molecule material was placed on both sides of the active layer, many combinations still achieved good device performance and yielded improved photostability of the device. This example fully demonstrates the uniqueness of the SAM material as a dual-functional interface material and opens up new avenues for the future development of high-performance SAM materials and the design of the device layer stack.

2. Results and Discussion

2.1. The Effects of SAMs Coated on ZnO

SAMs have been widely applied in inorganic perovskite solar cells and organic solar cells due to their high transparency, solubility in alcohol solvents, and low cost.[56–59] **Figure 1a** shows the structure of several small molecular organic acids of benzoic acid (BA), 4-chlorobenzoic acid (4-CBA), 1-naphthoic acid (1-NA), phenylphosphonic acid (PPA), and benzenesulfonic acid (BSA) were used for modifying the ZnO-active layer interface in this study. All SAM materials exhibited excellent solubility in alcohol solution, but they exhibited different pK_a values (**Table 1**), which were used to correlate the improvement in device efficiency with the pK_a. Figure 1b illustrates the variation in the work function (WF) of ZnO deposited on the ITO substrate before and after the modification with SAM materials. Obviously, while the 4-CBA yielded a considerable increase in work function upon modification, which might attributed to the displacement of its dipole caused by the presence of chlorine, the remaining SAM materials resulted in a lowering of the WF upon modification. This lowering is in fact beneficial for aligning the lowest unoccupied molecular orbital (LUMO) level of the acceptor in the photoactive material, which reduces the energy barrier for charge transfer and enhances the efficiency of charge extraction. Figure 1c presents the investigation of transmittance on ITO/ZnO and undergoing small molecule SAM treatment. All samples modified by SAM, except for 1-NA, exhibit optical absorption characteristics comparable to ITO/ZnO. This indicates that these substances do not consume too many photons before the spectrum reaches the active layer, thus do not cause significant negative effects on the short-circuit current. Since 1-NA did not yield large differences in film thickness, even not upon a large difference in concentration, the performance difference obtained is not significant, as shown in Figure S9 (Supporting Information). In Figure 1d and Figure S3 (Supporting Information) the water contact angles of all interface layers and the active layer are characterized. Among those samples, except for ITO/ZnO/BSA, which yielded the same results compared to the ITO/ZnO, other modified layers achieved increased contact angles. Similarly, the contact angle values of the active layer are also very large because the surface is

 © 2023 The Authors. Small Methods published by Wiley-VCH GmbH

23669608, 2024, 9, Downloaded from https://onlinelibrary.wiley.com/doi/10.1002/smtd.202301451 by Helmholtz-Zentrum Berlin Für, Wiley Online Library on [20/10/2025]. See the Terms and Conditions (https://onlinelibrary.wiley.com/terms-and-conditions) on Wiley Online Library for rules of use; OA articles are governed by the applicable Creative Commons License

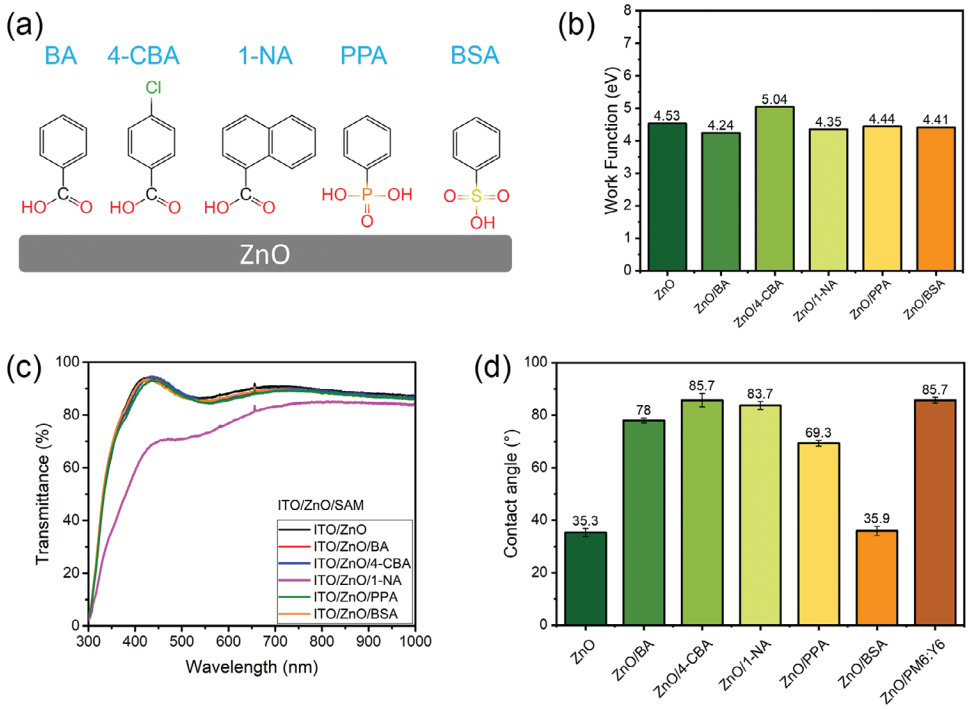

Figure 1. Chemical structure of SAM materials. b) Work function, c) Transmittance, and d) Contact angle results of ITO/ZnO and ITO/ZnO/SAM.

hydrophobic. Therefore, the increased contact angle is beneficial for achieving good contact with the active layer during its deposition, reducing the surface resistance. Atomic Force Microscopy (AFM) images of ZnO/SAM are shown in Figure S2 (Supporting Information), it is observed that the modified ZnO, exhibits a smoother film compared to bare ZnO. This is beneficial for achieving a better interface when depositing PM6:Y6 and reducing device resistance. To elucidate changes in the surface chemical bonds of SAMs after deposition on ZnO, X-ray photoelectron spectroscopy (XPS) was employed to conducted on the corresponding samples. **Figure 2** shows the high-resolution O 1s spectra of ZnO and the respective ZnO/SAM, where the two relevant peaks represent lattice oxygen (≈ 529.9 eV) and oxygen bound to carbon atoms (≈531.4 eV), respectively.[60] It is evident that after SAM modification, both O 1s peaks of ZnO shift toward higher binding energies, indicating enhanced coordination between the SAM and Zn^{2+} in ZnO/SAM.[61] Moreover, in the spectra of C 1s, S 2p, and P2p shown in Figures S4 and S5 (Supporting Information), significant enhancements of CO_2^-, SO_3^-, and PO_3^- signals were observed after SAM modification on ZnO, reflecting stronger interaction between these acid radicals and ZnO, which might weaken the residual —OH on the ZnO surface and mitigate its negative impact on the device during aging processes. Furthermore, the enhanced amount of aromatic C—C bonds and the presence of a S 2p and P 2p doublet for the ZnO/BSA and ZnO/PPA sample, respectively, is another confirmation for the successful SAM formation.

2.2. Solar Cells Performance Analysis

A series of solar cells using an inverted structure were fabricated, as shown in **Figure 3**a. All SAM's and ZnO conditions were optimized by exploring the different solution concentrations and annealing temperatures, as demonstrated in Figures S6–S11 and Tables S1–S6 (Supporting Information). It is worth noting that in the devices with a 1-NA, the concentrations range from 3 to 20 mg mL^{-1} to investigate its impact on device efficiency,

Table 1. SAMs pK_a value and photovoltaic performance of inverted OSCs based on ZnO and ZnO/SAM in combination with PM6:Y6 under illumination by an AM 1.5G solar simulator at a light intensity of 100 mW cm^{-2}. J_{sc} was corrected by the value of EQE.

ETL	pK_a	V_{oc} [V]	J_{sc}^{EQE} [mA cm^{-2}]	FF [%]	R_s [Ω]	PCE^{EQE} [%]
ZnO	/	0.855 ± 0.005	22.38 ± 0.91	61.0 ± 0.8	7.3 ± 0.5	11.72 ± 0.43
ZnO/BA	4.19[64]	0.859 ± 0.006	22.76 ± 0.59	65.0 ± 0.6	6.0 ± 0.6	12.67 ± 0.78
ZnO/4-CBA	3.98[64]	0.865 ± 0.004	23.31 ± 0.21	60.0 ± 0.4	6.5 ± 0.7	12.11 ± 0.49
ZnO/1-NA	3.70[65]	0.874 ± 0.002	23.31 ± 0.31	64.0 ± 0.5	6.8 ± 0.7	13.03 ± 0.44
ZnO/PPA	1.83[66]	0.873 ± 0.005	23.59 ± 0.54	63.5 ± 0.6	6.0 ± 0.5	13.06 ± 0.36
ZnO/BSA	−2.80[67]	0.874 ± 0.005	22.83 ± 0.36	63.8 ± 0.5	6.3 ± 0.5	12.79 ± 0.23

© 2023 The Authors. Small Methods published by Wiley-VCH GmbH

23669608, 2024, 9, Downloaded from https://onlinelibrary.wiley.com/doi/10.1002/smtd.202301451 by Helmholtz-Zentrum Berlin Für, Wiley Online Library on [20/10/2025]. See the Terms and Conditions (https://onlinelibrary.wiley.com/terms-and-conditions) on Wiley Online Library for rules of use; OA articles are governed by the applicable Creative Commons License

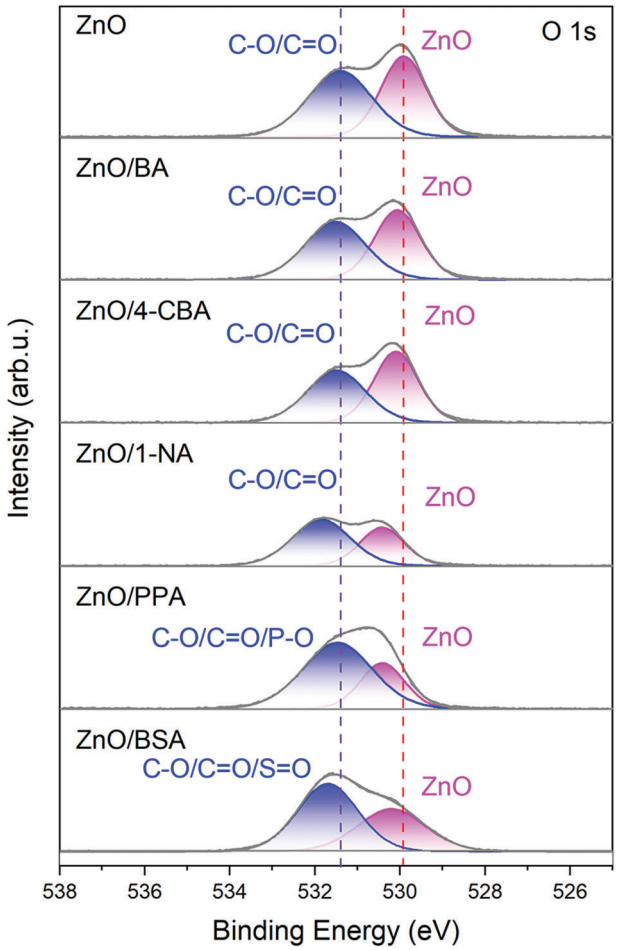

Figure 2. XPS results of O 1s core level for neat ZnO and ZnO/SAM films on the ITO substrate.

shown in Figure S12 (Supporting Information). It found that even though the concentration was set to 20 mg mL^{-1}, the material did not have a significant negative effect on the device efficiency, and still maintained a high performance of 12.7%. The *J–V* characterization curves and OSCs photovoltaic parameters including open circuit voltage (V_{oc}), short circuit current (J_{sc}), fill factor (FF), serial resistance (R_s), and power conversion efficiency (PCE) of bare ZnO and ZnO/SAM under optimal conditions are shown in Figure 3b and Table 1, respectively. The external quantum efficiency (EQE) spectrum (shown in Figure 3c) of the modified ZnO also exhibits a significant improvement in the 300 to 900 nm region, which is consistent with the trend of J_{sc}, shown in Table 1. The modified ZnO with a smoother surface resulted in a reduction in the surface resistance of the OSCs and also had a certain inhibitory effect on the leakage current, as shown in Figure 3d. The performance of the OSCs increased from 11.72% for the unmodified device to consistently over 12% for all SAM-based devices. Furthermore, OSCs containing 1-NA and PPA achieved an efficiency of over 13%, indicating the conspicuous of these SAMs in enhancing device performance. Typically, the annealing process decreases the V_{oc} of the device.[62] In order to establish a comparison between V_{oc} and WF, the device with the optimal condition of each SAM, but without annealing were employed. In Figure 3e and Table S7 (Supporting Information), the correlation between the V_{oc} and WF for devices and films fabricated under optimal conditions for both ZnO and ZnO/SAM, without thermal annealing. The WF of the films before and after ZnO modification shows the same trend as the corresponding V_{oc} obtained in the devices, providing guidance for achieving high V_{oc} in OSCs. Interestingly, the PCE of the devices after SAM modification shows a trend of initially increasing and then decreasing with the decrease in the SAM's own pK_a, shown in Figure 3f. The impact of the pK_a value of SAM on device efficiency may be attributed to the bonding rate, stability of SAM molecules with ZnO, and the coverage extent on ZnO. The deviation observed with 4-CBA is primarily due to the device exhibiting relatively poor V_{oc} and FF, shown in Table 1. The voltage loss is mainly attributed to the higher WF acquired by this material after modifying ZnO, causing a mismatch with the LUMO of the Y6. The lower FF may result from its more hydrophobic surface, which tends to enrich the more hydrophobic PM6 than Y6,[63] forming a vertical phase structure with a relatively higher proportion of PM6 than other ZnO/SAM. This structure is less favorable for charge transport in the inverted device architecture, leading to a relatively lower FF and efficiency. This arrangement between PCE and pK_a provides valuable insights for finding advisable modifying materials for this system. Based on this strategy, and applied it to the widely used non-fullerene system PBDB-T:ITIC and presented the results in Figure S13 and Table S8. The device results exhibited a similar trend to PM6:Y6, where most SAMs improved the device performance. It indicates the potential of extending this method to other organic solar cell systems.

The average parameters were obtained from four solar cells.

2.3. Charge Recombination, Dissociation, and Extraction Properties

In order to further investigate the influence of introducing SAM on charge recombination in the device, light intensity dependence on V_{oc} and J_{sc} was estimated.[68] The relationship between J_{sc} and light intensity is denoted as $J_{sc} \propto (P_{light})^{\alpha}$, where J_{sc} represents the short-circuit current of the device, and P_{light} corresponds to the light intensity of the applied solar simulator. When α approaches 1, it indicates that there is a small degree of bimolecular recombination in the device. Therefore, in **Figure 4a**, after SAM modification, the α values show a slight improvement relative to the devices containing only ZnO. This indicates that the various SAM modifications have no significant negative effects on the bimolecular recombination in the devices. Additionally, the relationship between V_{oc} and light intensity is described as $V_{oc} = n(k_B T/q)\cdot\ln(P_{light})$, where V_{oc} represents the open-circuit voltage of the OSCs, k_B is the Boltzmann constant, T is the absolute temperature, q represents the elementary charge, and P_{light} represents the incident light intensity of OSCs. In this case, the calculated value of n generally ranges from 1 to 2. When it is close to 1, it indicates that bimolecular recombination is dominant in the OSCs. When it approaches 2, it suggests that monomolecular recombination, respectively trap-assisted charge recombination is dominant in the device. In Figure 4b, the results obtained from the fitting show that the device modified with SAM

 © 2023 The Authors. Small Methods published by Wiley-VCH GmbH

23669608, 2024, 9, Downloaded from https://onlinelibrary.wiley.com/doi/10.1002/smtd.202301451 by Helmholtz-Zentrum Berlin Für, Wiley Online Library on [20/10/2025]. See the Terms and Conditions (https://onlinelibrary.wiley.com/terms-and-conditions) on Wiley Online Library for rules of use; OA articles are governed by the applicable Creative Commons License

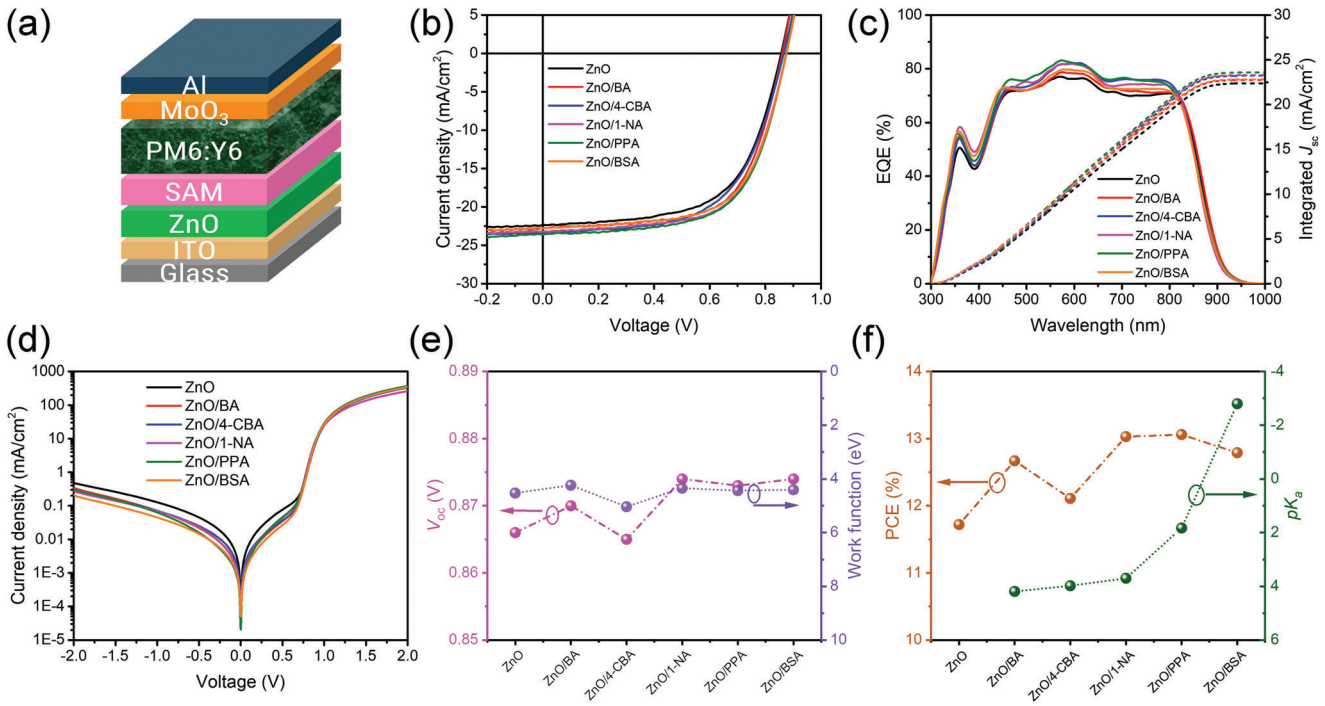

Figure 3. a) Layer stack for OSCs, b) *J–V* characterization performed under an AM 1.5G solar simulator, c) EQE spectra analysis, d) Dark *J–V* curves, e) Averaged work function and V_{oc} values of ZnO and ZnO/SAM-based inverted OSCs (without thermal annealing), and f) Averaged PCE values of OSCs modified with different SAM and SAM's pK_a value.

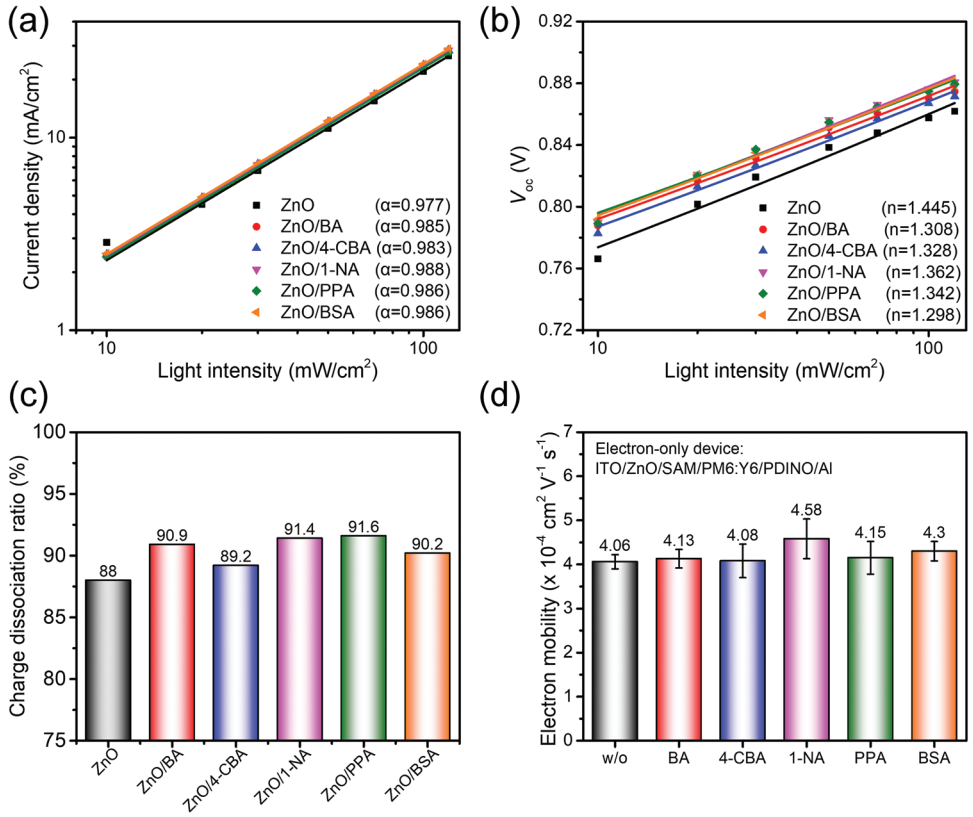

Figure 4. Light intensity dependence of a) J_{sc}, b) V_{oc}, c) Charge dissociation ratio measured by J_{ph} versus V_{eff} curves, and d) Electron mobility of devices based on bare ZnO and ZnO/SAM.

 © 2023 The Authors. Small Methods published by Wiley-VCH GmbH

23669608, 2024, 9, Downloaded from https://onlinelibrary.wiley.com/doi/10.1002/smtd.202301451 by Helmholtz-Zentrum Berlin Für, Wiley Online Library on [20/10/2025]. See the Terms and Conditions (https://onlinelibrary.wiley.com/terms-and-conditions) on Wiley Online Library for rules of use; OA articles are governed by the applicable Creative Commons License

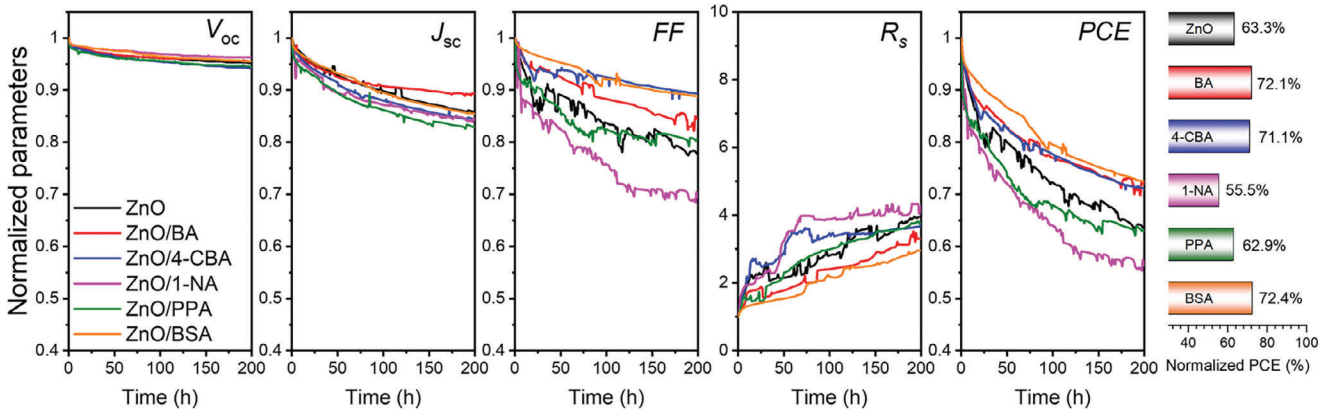

Figure 5. Normalized photovoltaic parameters V_{oc}, J_{sc}, FF, R_s and PCE for OSCs fabricated using bare ZnO and ZnO/SAM were determined under ISOS-L1 condition, which included exposure to 1 sun LED and a temperature of 45°C. The averaged data of photovoltaic parameters are from at least two solar cells.

exhibits a smaller n value present a weaker trap-assisted recombination compared to the device with only ZnO, indicating that the addition of this SAM material plays a suppressing role in inhibiting defect complexation of the device. The OSCs obtained smaller trap-assisted and monomolecular recombination upon ZnO modification by SAM. To further study the charge dissociation property in the device, the relationship between the photocurrent density (J_{ph}) and the effective voltage (V_{eff}) was investigated and is shown in the supporting information. The photocurrent, defined as $J_L - J_D$, is the difference between the J_{sc} obtained by the same device under AM 1.5 illumination and in the dark, respectively. The V_{eff} is expressed as $V_{o-} V_{appl}$, where V_o is the voltage at which J_D and J_L are equal, and V_{appl} is the applied voltage. P_{diss} is the ratio of J_{ph} to saturation current density (J_{sat}). The J_{sat} is revealed at V = 3 V, where it is assumed that all electron-hole pairs are completely dissociated and extracted by the top and bottom electrodes.[69] In Figure 4c and Figure S14 (Supporting Information), it is observed that after SAM treatment, the charge dissociation efficiency in the device is improved to varying degrees compared to the device with only ZnO. It indicates that SAM modification can effectively promote the dissociation of charges within the device, which is beneficial for enhancing the J_{sc} and FF of the OSCs. To further disentangle the impact of SAM on the electron mobility behavior in the device, the electron-only OSCs with a layer stack of ITO/ZnO/SAM/PM6:Y6/PDINO/Al were fabricated. The *J-V* curve of the devices was measured in a dark environment, and the mobility was calculated using the space-charge-limited current (SCLC) method,[70] and the results are shown in Figure 4d and Figure S15 (Supporting Information). After SAM modification, it was observed that the electron mobility, respectively the current, of the devices slightly increased. This indicates improved charge injection and extraction by the electrodes.

2.4. Devices Stability Characterization

To elucidate the effect of SAM-modified ZnO on the photo stability of the device, the glass-encapsulated devices were exposed to an aging experiment under conditions defined by the international summit on organic photovoltaic stability light soaking level 1 (ISOS-L1).[71] After 200 h of LED irradiation at 45°C, the photovoltaic parameters of the device showed different trends, as shown in **Figure 5**. V_{oc} maintained good stability, which may be mainly influenced by the active material. However, J_{sc} and FF exhibited different decay progression, which might be related to the impact of the interface layer on the active layer. The device photostability was improved after the modification with BA, 4-CBA, and BSA. This might be attributed to the effective reduction of —OH content on ZnO through the modification of these SAMs. The lone pair electrons on the —OH groups can attack the C=C bonds of the fullerene acceptor terminal groups, leading to a decrease in device stability.[46] PPA-modified devices exhibit similar stability to the original ZnO devices, which may be attributed to the uniqueness of the phosphonic acid functional group. In general, phosphonic acid groups form stable multi-dentate binding structures with ZnO,[72] reducing the presence of —OH groups on the ZnO surface. However, the results indicate that the device modified with PPA achieves slightly lower stability than ZnO, and the underlying cause of this phenomenon remains unclear. In contrast, devices with 1-NA exhibits mediocre stability, possibly due to the generation of numerous oxidative substances when it interacts with ZnO under illumination conditions.[73] These substances can easily penetrate into the active layer, causing oxidation and degradation of the active layer material, thus reducing the stability of the device. Meanwhile, the electroluminescence imaging (ELI) and photoluminescence (PL) spectra of the devices before and after aging were performed, shown in Figures S16 and S17 (Supporting Information), respectively. After 200 h of aging under ISOS-L1 conditions, ZnO-only device exhibited a high-density range of defect black spots. In contrast, the s with SAM showed relatively smaller increases in defect quantity and expansion of existing defects. However, the differences in PL spectra of the same device before and after aging are significant. BA, 4-CBA, and BSA contented device maintained a relatively high level of compared to the original spectrum, indicating their good protective effect on the device after 200 h aging. However, the 1-NA and PPA contained device remained relatively low compared to ZnO, indicating their ability to improve device stability or protect the active layer is insufficient. In Figure S18 (Supporting Information), the structure of ITO/ZnO/SAM/PM6:Y6/Glue/Glass was

 © 2023 The Authors. Small Methods published by Wiley-VCH GmbH

23669608, 2024, 9, Downloaded from https://onlinelibrary.wiley.com/doi/10.1002/smtd.202301451 by Helmholtz-Zentrum Berlin Für, Wiley Online Library on [20/10/2025]. See the Terms and Conditions (https://onlinelibrary.wiley.com/terms-and-conditions) on Wiley Online Library for rules of use; OA articles are governed by the applicable Creative Commons License

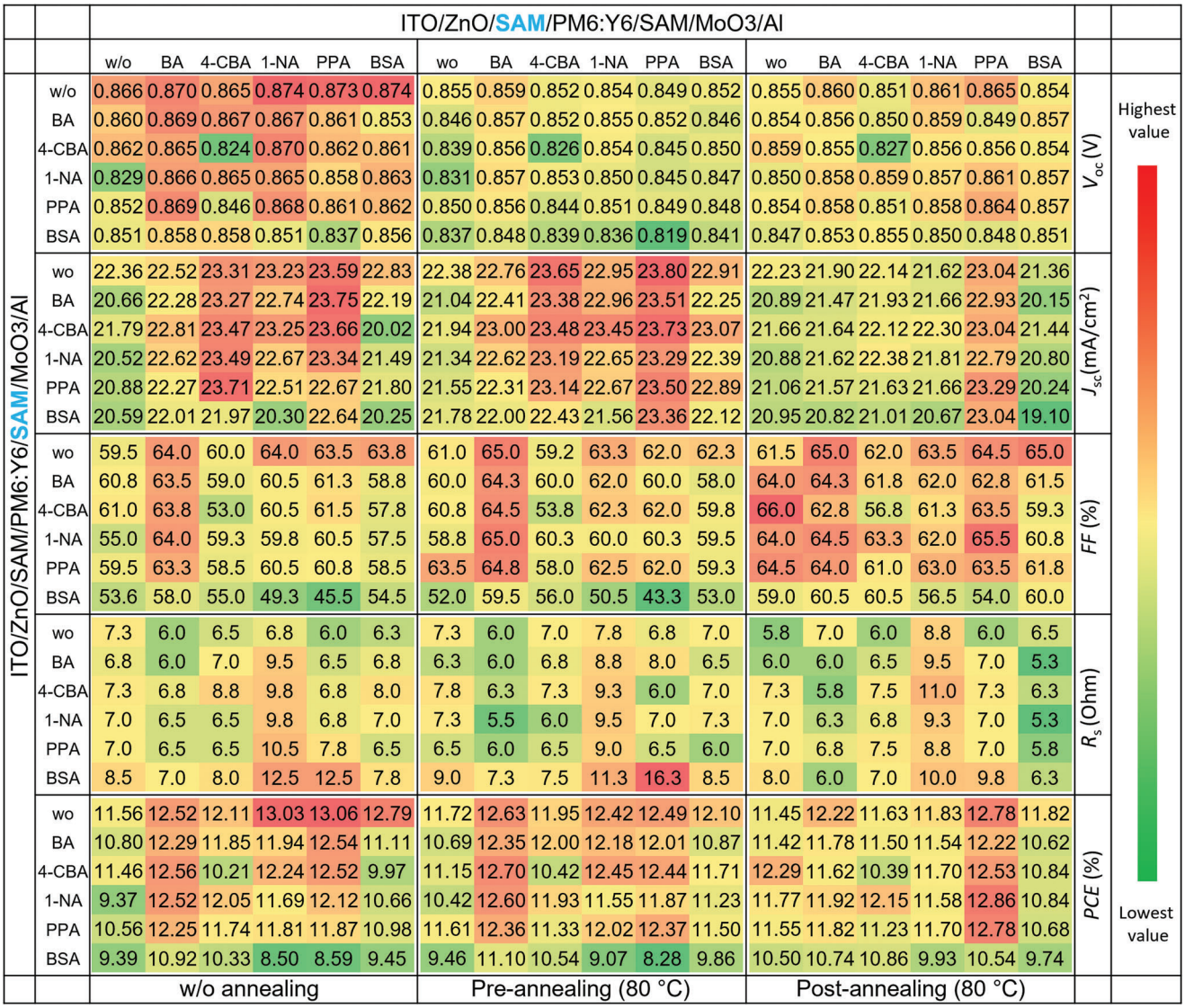

Figure 6. The photovoltaic parameters including J_{sc}, V_{oc}, FF, R_s, and PCE were determined for the dual-SAM device composed of ITO/ZnO/SAM/PM6:Y6/SAM/MoO_3/Al. The SAM between ZnO and PM6:Y6 is represented horizontally, while the SAM between PM6:Y6 and MoO_3 is represented vertically.

used to investigate the effect of SAM introduction by measuring the absorptance with different aging time on the stability of the active layer. During the aging process, the main peak positions of the PM6 and Y6 spectra showed signs of attenuation. After prolonged illumination, the differences in their ability to protect the activity gradually became evident. Their ability to protect the photoactive layer is also similar to the device's photostability.

2.5. Devices Performance and Stability Characterization for Dual-Use SAM Application

It has been confirmed that in OSCs, MoO_3 can decompose under light conditions and float into the active layer, causing the phenomenon of rapid device stability attenuation.[74–77] Organic acid-based SAM materials can be used as both the conventional structure's HTL layer and the inverted structure's ZnO modification layer. Therefore, SAMs were implemented on both sides of the active layer, aiming to further enhance the stability of the device. Additionally, the design of using the same SAM material in different positions of the device as different functional layers is also filled with unknowns. A series of devices were systematically fabricated using the orthogonal method to study the effects of double SAM layers on device performance. The *J-V* curves, EQE curves, and photovoltaic performance parameters are shown in Figures S19–S23 and Table S9–S13 (Supporting Information). Additionally, the photovoltaic parameters are displayed in **Figure 6** with three-color scales. After comprehensive research, it is possible to identify the impact of SAM combinations on device performance, as well as the effects of pre-annealing and post-annealing on the photovoltaic parameters of the OSCs. In Figure 6, most of the V_{oc} values

 © 2023 The Authors. Small Methods published by Wiley-VCH GmbH

23669608, 2024, 9, Downloaded from https://onlinelibrary.wiley.com/doi/10.1002/smtd.202301451 by Helmholtz-Zentrum Berlin Für, Wiley Online Library on [20/10/2025]. See the Terms and Conditions (https://onlinelibrary.wiley.com/terms-and-conditions) on Wiley Online Library for rules of use; OA articles are governed by the applicable Creative Commons License

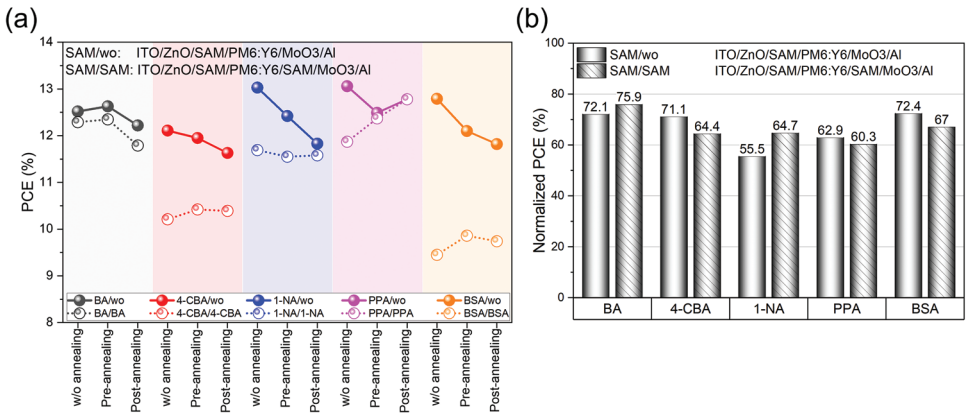

Figure 7. a) PCE trends under different processing conditions and b) photostability histograms based on champion devices for single and dual SAMs of the same material.

for various combinations are almost equivalent, except that they decrease after thermal annealing. In terms of J_{sc}, the devices with 4-CBA (or PPA)/PM6:Y6/SAM exhibit higher J_{sc}, and this improvement is maintained or even further enhanced after pre-annealing treatment. Regarding FF, SAM/PM6:Y6/wo and BA/PM6:Y6/SAM reveal better results. After annealing, all devices demonstrate varying degrees of improvement in FF, with particularly noticeable enhancement after post-annealing. In terms of R_s, SAM/PM6:Y6/wo and BA/PM6:Y6/SAM also exhibit lower R_s in the devices. After annealing, only the devices with the SAM/PM6:Y6/wo combination maintain lower R_s. Interestingly, the devices with the BSA/PM6:Y6/SAM combination show significant improvement in R_s after post-annealing. For PCE, devices with the SAM/PM6:Y6/wo and BA/PM6:Y6/SAM combinations exhibit higher PCE values. After pre-annealing, the devices with SAM/PM6:Y6/wo as the base maintain a superior PCE. Furthermore, the devices with the PPA/PM6:Y6/SAM combination demonstrate consistently high device efficiency after post-annealing. In this result, although devices with the SAM/PM6:Y6/SAM combination initially exhibit relatively lower device performance compared to devices with the SAM/PM6:Y6/wo combination, most devices catch up after pre-annealing or post-annealing treatments. Although SAM does not demonstrate superior device efficiency in the ITO/ZnO/PM6:Y6/SAM/MoO_3/Al structure compared to the ZnO-only device, it plays a role in enhancing device efficiency when subjected to post-annealing or when combined with ZnO/SAM. This indicates that the design of the dual-SAM device can still achieve excellent performance.

To identify the impact of double-SAM on the stability of the device, the photostability of the relevant encapsulated devices under conditions of ISOS-L1 were performed, and the results are shown in (Figures S25 and S26, Supporting Information). After the introduction of the upper SAM and different ZnO modification layers, the stability of the devices showed a relatively random phenomenon. However, the dual-SAM devices with ZnO/4-CBA or BSA showed decreased performance after the introduction of SAM above the active layer, compared to the devices that were only modified with ZnO, which exhibited decreased device stability. It is worth noting that in dual-SAM devices based on ZnO/BA or ZnO/1-NA, the introduction of the upper SAM has improved device stability to varying degrees. When introducing these SAMs between the active layer and HTL, the dual-SAM devices exhibited different effects on device photostability. This may be attributed to the ability of these materials to enhance the photostability of MoO_3 or suppress the diffusion of MoO_3 into the active layer. Interestingly, in **Figure** 7a, Although all of SAM/SAM showed varying reductions in device efficiency compared to ZnO/SAM, the BA/BA (Pre-annealing at 80°C) and PPA/PPA (Post-annealing at 80°C) pairs still maintained a high and relatively comparable device performance. Among the dual SAM combinations, the use of BA and PPA as modifying layers for ZnO is more suitable, achieving higher device efficiency. Notably, the stability of the BA-based configuration outperforms that of PPA, as illustrated in Figure S26 (Supporting Information). Therefore, considering both efficiency and stability, the BA/4-CBA combination within the ZnO/BA-based configuration exhibits not only high efficiency but also superior stability, establishing itself as the most favorable dual SAM combination among these configurations. In Figure 7b, except for the BA/BA and 1-NA/1-NA combinations, the other three combinations of the same SAM/SAM pairs showed lower photostability compared to using a single SAM. Importantly, the dual-SAM devices with the same BA or 1-NA demonstrated improved stability compared to using a single type of SAM. These results demonstrate the possibility of applying the same material in different locations in the same device, providing a new design strategy for achieving high-efficiency and high-stability OSCs.

3. Conclusion

In this work, we selected five structurally similar organic acid small molecules as SAMs to investigate their effects on device performance after introducing them into the PM6:Y6-based system by modifying ZnO. After modification, the surface became more homogeneous, and the devices exhibited reduced bimolecular and trap-assisted recombination, leading to improved device J_{sc} and FF, thus achieving better device efficiency. The stability of the devices modified with BA, BSA, and 4-CBA showed certain improvements under ISOS-L1 conditions, while the stability of the devices modified with 1-NA and PPA alone was relatively lower than that of only ZnO. Moreover, these SAMs also played a

© 2023 The Authors. Small Methods published by Wiley-VCH GmbH

23669608, 2024, 9, Downloaded from https://onlinelibrary.wiley.com/doi/10.1002/smtd.202301451 by Helmholtz-Zentrum Berlin Für, Wiley Online Library on [20/10/2025]. See the Terms and Conditions (https://onlinelibrary.wiley.com/terms-and-conditions) on Wiley Online Library for rules of use; OA articles are governed by the applicable Creative Commons License

role in improving device efficiency in the PBDB-T:ITIC system, providing some support for the extended application of these SAMs. Interestingly, it was observed that incorporating SAM located at both sides of active layer allowed some devices to maintain better device performance compared to the ZnO/SAM devices. More specifically, when the same SAM was simultaneously applied to the device, some SAMs exhibit comparable PCE to ZnO/SAM and even enhanced stability. This dual application of the same material in the device layer structure design provides some feasible approaches for future designs of high-performance and highly stable OSCs.

4. Experimental Section

Materials: The Glass/ITO substrate was obtained from Xinyan Technology co, Limited (Taiwan, China). The hole transport layer PEDOT:PSS (Clevios PH) was acquired from Heraeus (Hanau, Germany). Zinc acetate dihydrate (99.5+%) was procured from ChemPUR (Karlsruhe, Germany). Chloroform, 1-chloronaphthalene, 2-aminoethanol (>99%), 2-methoxyethanol, and methanol were received from Sigma Aldrich. Benzoic acid (99%), 4-chlorobenzoic acid (98%+), 1-naphthoic acid (98%), phenylphosphonic acid (98%), and benzenesulfonic acid (94%) were purchased from Alfa Aesar (Kandel, Germany). Poly[(2,6-(4,8-bis(5-(2-ethylhexyl-3-fluoro)thiophen-2-yl)-benzo[1,2-b:4,5-b']dithiophene))-alt-(5,5-(1′,3′-di-2-thienyl-5′,7′-bis(2-ethylhexyl)benzo[1′,2′-c:4′,5′-c']dithiophene-4,8-dione)] (PM6), 2,2′-((2Z,2′Z)-((12,13-bis(2-ethylhexyl)−3,9-diundecyl-12,13-dihydro-[1,2,5]thiadiazolo[3,4-e]thieno[2″,3′′:4′,5′]thieno[2′,3′:4,5]pyrrolo[3,2-g]thieno[2′,3′:4,5]thieno[3,2-b]indole-2,10-diyl)bis(methanylylidene))bis(5,6-difluoro-3-oxo-2,3-dihydro-1H-indene-2,1-diylidene))dimalononitrile (Y6), poly[[4,8-bis[5-(2-ethylhexyl)−2-thienyl]benzo-[1,2-b:4,5b']dithiophene-2,6-diyl]−2,5-thiophenediyl[5,7-bis(2-ethylhexyl)−4,8-dioxo-4H,8H-benzo[1,2-c:4,5-c']dithiophene-1,3-diyl]] (PBDB-T), and 3,9-bis(2-methylene-(3-(1,1-dicyanomethylene)-indanone))−5,5,11,11-tetrakis(4-hexylphenyl)-dithieno[2,3-d:2′,3′-d']-s indaceno[1,2-b:5,6-b']dithiophene (ITIC) were purchased from Brilliant Matters (Quebec City, Canada). Aluminum and MoO_3 were purchased from Kurt J. Lesker (Dresden, Germany).

Device Fabrication: The patterned ITO/Glass substrate was cleaned by wiping the surface with a cotton swab dipped in toluene, and then subjected to two rounds of ultrasound using toluene and isopropanol for 15 min, respectively, in a 40°C water. The pre-treated ITO/Glass substrate is further dried with nitrogen gas and then subjected to plasma (Argon) treatment for 5 min to increase its surface wettability. The precursor solution of ZnO is spin-coated onto the treated ITO/Glass surface in ambient air conditions (5000 rpm, 45 s), with each substrate receiving 100 µL of the solution. Subsequently, it is transferred to a hot plate for annealing at 178°C for 45 min. After annealing, the sample is immediately transferred to a glove box filled with nitrogen atmosphere to cool down to room temperature. The modifying layer solution is dissolved in methanol and deposited onto the cooled ZnO with different concentrations and spin frequencies. The active layer, consisting of PM6 and Y6 with a mass ratio of 1:1.2 and a total concentration of 16 mg mL^{-1}, is dissolved in chloroform and stirred at 50°C for at least 2 weeks with the addition of 0.5% volume ratio of 1-chloronaphthalene. The PM6:Y6 blend solution is spin-coated onto the ZnO or modifying layer (SAM) at a spin-frequency of 2000 rpm for 30 s. The PBDB-T:ITIC blend, consisting of a 1:1 weight ratio, is dissolved in chlorobenzene with a concentration of 16 mg mL^{-1}. 0.5 vol% of 1,8-diiodooctane was added as an additive, and the mixture was stirred for a minimum of three weeks at 50°C. The PBDB-T:ITIC film was deposited on top of ZnO or ZnO/SAM at a spin frequency of 2000 rpm for 30 s and then subjected to a heat treatment at 150°C for 10 min. After that, different heating conditions are chosen for the thermal annealing of the samples. Once the treatment is completed, the samples are transferred to a vacuum chamber for physical vapor deposition under a vacuum of 5×10^{-6} mbar to deposit a 10 nm of MoO_3 and a 200 nm of aluminum. During deposition, a grid mask was used to determine the final area of the solar cells, which is 0.42 cm^2. Subsequently, the devices with electrode deposition undergo thermal annealing under different conditions. Finally, the devices are sealed by adding drops of UV epoxy resin on top of the aluminum electrode, covering it with a glass slide, and then subjected to device encapsulation using UV lamps.

Characterization: The encapsulated solar cells were measured short circuit current density-voltage (*J–V*) curves using an AM 1.5G solar simulator (Wavelabs, Sinus-70) for both light and dark conditions in the air. External quantum efficiency (EQE) curves were performed using monochromatic light and additional halogen bias light provides ≈1 sun excitation intensity, the wavelength is from 300 to 1000 nm. Atomic force microscopy (AFM) was obtained by JPK Nanowizard 4 (Bruker) with tapping mode in air ambient. The water contact angle of films was measured by the contact angle set up (DataPhysics Instruments GmbH, Germany) at the three-phase point liquid/solid/air at room temperature, 3 µL water was applied for each measurement. X-ray photoelectron spectroscopy (XPS) measurements using a K-Alpha X-ray Photoelectron Spectrometer System (Thermo Fisher Scientific) with a monochromatic X-ray source (Al Kα) with a spot diameter of 400 µm and an electron detector with 0.5 eV energy resolution. The spectra were calibrated using the C 1s peak (284.6 eV) and fitted using Voigt functions after Shirley background subtraction. The work function (WF) of the bare ITO and the modification layer was performed by a single-point Kelvin probe system (Anfatec Instruments AG, Germany) at room temperature in the air. UV–vis-NIR spectra of The reflection and transmission were acquired by a spectrophotometer (Avantes AvaSpec-ULS3648-USB2-UA-25) with a wavelength from 300 to 1200 nm. Photoluminescence (PL) spectra were recorded using AvantesAvaSpecULS-2048 fiber spectrometer from 500 to 1100 nm, and the excitation wavelength of 405 nm was applied.

The device's stability was carried out utilizing the condition of an international summit on organic photovoltaic stability light soaking level 1 (ISOS-L1, 45°C) under the LED array with the light intensity of 100 mW cm^{-2} in air. During adding process, the Keithley 2400 SMU and a Keithley 2700 multiplexer were used to collecting the *J–V* curves and extract photovoltaic data every 30 min. Electroluminescence imaging (ELI) is performed to investigate the solar cells' inhomogeneity and a Keithley 2400 SMU was employed to a current of 20 mA during each measurement in dark environment in an ambient. The Si CCD camera (ANDOR iKon-M) was applied to capture the emitted light from the solar cells after cooling down to −50°C.

The mobility was carried with a hole-only device with the layer stack of ITO/PEDOT:PSS/active layer/(SAM)/MoO_3/Al, and an electron-only device with the layer structure of ITO/ZnO/SAM/active layer/PDINO/Al, respectively. *J–V* curves of relevant devices were measured under dark conditions and fitted according to the model of space charge limited current (SCLC), described by the MOTT-Gurney Equation: $J_D = 9\epsilon_0\epsilon_r\mu V^2/8L^3$, where the J_D is the current density, ϵ_0 is defined as the vacuum permittivity ($\epsilon_0 = 8.85$ C V^{-1} s^{-1}), ϵ_r is the relative permittivity of the material (for polymer system, presumed to be 3), μ is the mobility, V defined as $V_{appl} - V_{bi} - V_s$. V_{appl}, V_{bi}, and V_s are described as the applied voltage, built-in voltage (0 V), and the voltage drop result from the substrate's series resistance (for the electron-only device, the $V_s = 0$, while the hole-only device, $V_s = IR$), respectively. L is the thickness of the photosensitive layer.

Supporting Information

Supporting Information is available from the Wiley Online Library or from the author.

Acknowledgements

The authors gratefully acknowledge Susanne Sandkuhl for the AFM measurement. Z.X. was financially supported by the China Scholarship Council (CSC). H.H. is grateful for financial support from the Deutsche Forschungsgemeinschaft (DFG) via the DFG project number 431903417.

 © 2023 The Authors. Small Methods published by Wiley-VCH GmbH

23669608, 2024, 9, Downloaded from https://onlinelibrary.wiley.com/doi/10.1002/smtd.202301451 by Helmholtz-Zentrum Berlin Für, Wiley Online Library on [20/10/2025]. See the Terms and Conditions (https://onlinelibrary.wiley.com/terms-and-conditions) on Wiley Online Library for rules of use; OA articles are governed by the applicable Creative Commons License

U.S.S. is grateful to the Thüringer Ministerium für Wirtschaft, Wissenschaft und Digitale Gesellschaft (TMWWDG) for funding the CEEC Jena. A part of the equipment used in this study was obtained within the "RIS3 Innovation Center CEEC Jena" project funded by the Free State of Thuringia under number 2016 IZN 0009 and co-financed by funds from the European Union within the framework of the European Regional Development Fund (ERDF). U.S.S and A.T. acknowledge support by the European Fonds for Regional Development (Europäischer Fonds für Regionale Entwicklung; EFRE-OP 2014–2020; Project No. 2021 FGI 0035, NanoLabXPS) as part of the REACT-EU program. C.N. and A.T. acknowledge financial support by the DFG within the CRC-TRR 234 "CataLight" projects B07 and Z02.

Open access funding enabled and organized by Projekt DEAL.

Conflict of Interest

The authors declare no conflict of interest.

Data Availability Statement

The data that support the findings of this study are available in the supplementary material of this article.

Keywords

modification layer, organic solar cells, photostability, self-assembled monolayer

Received: October 20, 2023
Revised: December 15, 2023
Published online: December 31, 2023

[1] Y. Li, *Acc. Chem. Res.* **2012**, *45*, 723.
[2] L. Lucera, F. Machui, P. Kubis, H. D. Schmidt, J. Adams, S. Strohm, T. Ahmad, K. Forberich, H.-J. Egelhaaf, C. J. Brabec, *Energy Environ. Sci.* **2016**, *9*, 89.
[3] H. Jinno, K. Fukuda, X. Xu, S. Park, Y. Suzuki, M. Koizumi, T. Yokota, I. Osaka, K. Takimiya, T. Someya, *Nat. Energy.* **2017**, *2*, 780.
[4] M. Vilkman, K.-L. Väisänen, P. Apilo, R. Po, M. Välimäki, M. Ylikunnari, A. Bernardi, T. Pernu, G. Corso, J. Seitsonen, S. Heinilehto, J. Ruokolainen, J. Hast, *ACS Appl. Energy Mater.* **2018**, *1*, 5977.
[5] M. Rawat, E. Jayaraman, S. Balasubramanian, S. S. K. Iyer, *Adv. Mater. Technol.* **2019**, *4*, 1900184.
[6] E. Dauzon, X. Sallenave, C. Plesse, F. Goubard, A. Amassian, T. D. Anthopoulos, *Adv. Mater.* **2021**, *33*, 2101469.
[7] E. N. Güler, A. Distler, R. Basu, C. J. Brabec, H.-J. Egelhaaf, *Flex. Print. Electron.* **2022**, *7*, 025003.
[8] J. Cao, L. Yi, L. Zhang, Y. Zou, L. Ding, *J. Mater. Chem. A* **2023**, *11*, 17.
[9] Z. Chen, J. Zhu, D. Yang, W. Song, J. Shi, J. Ge, Y. Guo, X. Tong, F. Chen, Z. Ge, *Energy Environ. Sci.* **2023**, *16*, 3119.
[10] Y. Gao, X. Yang, W. Wang, R. Sun, J. Cui, Y. Fu, K. Li, M. Zhang, C. Liu, H. Zhu, X. Lu, J. Min, *Adv. Mater.* **2023**, *35*, 2300531.
[11] K. Liu, Y. Jiang, F. Liu, G. Ran, F. Huang, W. Wang, W. Zhang, C. Zhang, J. Hou, X. Zhu, *Adv. Mater.* **2023**, 2300363.
[12] S. Bishnoi, R. Datt, S. Arya, S. Gupta, R. Gupta, W. C. Tsoi, S. N. Sharma, S. P. Patole, V. Gupta, *Adv. Mater. Interfaces* **2022**, *9*, 2101693.
[13] J. Hu, W. Fu, X. Yang, H. Chen, *J. Polym. Sci.* **2022**, *60*, 2175.
[14] J. Jin, Q. Wang, K. Ma, W. Shen, L. A. Belfiore, X. Bao, J. Tang, *Adv. Funct. Mater.* **2023**, *33*, 2213324.
[15] J. Niederhausen, K. A. Mazzio, R. W. Macqueen, *Electron. Struct.* **2021**, *3*, 033002.
[16] H. Tang, Y. Bai, H. Zhao, X. Qin, Z. Hu, C. Zhou, F. Huang, Y. Cao, *Adv. Mater.* **2023**, 2212236.
[17] H. Xu, F. Yuan, D. Zhou, X. Liao, L. Chen, Y. Chen, *J. Mater. Chem. A* **2020**, *8*, 11478.
[18] X. Zhang, H. Zhang, Y. Li, S.-U. Zafar, S. Yang, J. Chen, H. Zhou, Y. Zhang, *Adv. Funct. Mater.* **2022**, *32*, 2205398.
[19] Q. Fan, R. Ma, J. Yang, J. Gao, H. Bai, W. Su, Z. Liang, Y. Wu, L. Tang, Y. Li, Q. Wu, K. Wang, L. Yan, R. Zhang, F. Gao, G. Li, W. Ma, *Angew. Chem., Int. Ed.* **2023**, *36*, e202308307.
[20] B. A. E. Courtright, S. A. Jenekhe, *ACS Appl. Mater. Interfaces* **2015**, *7*, 26167.
[21] P. Li, B. Wu, Y. C. Yang, H. S. Huang, X. D. Yang, G. D. Zhou, Q. L. Song, *Sol. Energy* **2018**, *170*, 212.
[22] X. Li, W. Zhang, K. Usman, J. Fang, *Adv. Energy Mater.* **2018**, *8*, 1702730.
[23] A. Sokeng Djoumessi, A. Sichwardt, D. Miliaieva, J. Cermák, M. Schaal, F. Otto, S. Stehlík, J. Kulicek, V. Nádazdy, T. Fritz, A. Kromka, B. Rezek, U. S. Schubert, H. Hoppe, *Sol. RRL* **2023**, *7*, 2201061.
[24] J. Zhao, Y. Li, G. Yang, K. Jiang, H. Lin, H. Ade, W. Ma, H. Yan, *Nat. Energy.* **2016**, *1*, 15027.
[25] A. Sokeng Djoumessi, S. Alam, J. P. Madalaimuthu, A. Anand, J. Slowik, T. Pflug, R. Meitzner, R. Roesch, E. Gnecco, A. Horn, U. S. Schubert, H. Hoppe, *Energy Technol.* **2021**, *9*, 2100474.
[26] A. Anand, M. M. Islam, R. Meitzner, U. S. Schubert, H. Hoppe, *Adv. Energy Mater.* **2021**, *11*, 2100875.
[27] A. Anand, J. P. Madalaimuthu, M. Schaal, F. Otto, M. Gruenewald, S. Alam, T. Fritz, U. S. Schubert, H. Hoppe, *ACS Appl. Electron. Mater.* **2021**, *3*, 929.
[28] L. Hu, J. Song, X. Yin, Z. Su, Z. Li, *Polymers* **2020**, *12*, 145.
[29] Y. H. Kim, C. Sachse, M. L. Machala, C. May, L. Müller-Meskamp, K. Leo, *Adv. Funct. Mater.* **2011**, *21*, 1076.
[30] D. Alemu, H.-Y. Wei, K.-C. Ho, C.-W. Chu, *Energy Environ. Sci.* **2012**, *5*, 9662.
[31] E. A. A. Arbab, G. T. Mola, *Appl. Phys. A* **2016**, *122*, 405.
[32] Y. Lee, S. Biswas, H. Kim, *Thin Solid Films* **2022**, *746*, 139134.
[33] B. Johnev, M. Vogel, K. Fostiropoulos, B. Mertesacker, M. Rusu, M.-C. Lux-Steiner, A. Weidinger, *Thin Solid Films* **2005**, *488*, 270.
[34] B. Johnev, K. Fostiropoulos, *Sol. Energy Mater. Sol. Cells* **2008**, *92*, 393.
[35] M. Rusu, S. Wiesner, I. Lauermann, C.-H. Fischer, K. Fostiropoulos, J. N. Audinot, Y. Fleming, M. C. Lux-Steiner, *Appl. Phys. Lett.* **2010**, *97*, 073504.
[36] I. Bochukov, W. Schindler, B. Johnev, T. Mete, K. Fostiropoulos, *Chem. Phys. Lett.* **2011**, *511*, 363.
[37] K. Fostiropoulos, M. Rusu, *Sol. Energy Mater. Sol. Cells* **2011**, *95*, 1489.
[38] N. Beaumont, I. Hancox, P. Sullivan, R. A. Hatton, T. S. Jones, *Energy Environ. Sci.* **2011**, *4*, 1708.
[39] X. Zhu, B. Guo, J. Fang, T. Zhai, Y. Wang, G. Li, J. Zhang, Z. Wei, S. Duhm, X. Guo, M. Zhang, Y. Li, *Org. Electron.* **2019**, *70*, 25.
[40] K. Borse, R. Sharma, D. Gupta, A. Yella, *RSC Adv.* **2018**, *8*, 5984.
[41] Z. Liang, Q. Zhang, O. Wiranwetchayan, J. Xi, Z. Yang, K. Park, C. Li, G. Cao, *Adv. Funct. Mater.* **2012**, *22*, 2194.
[42] B. R. Lee, E. D. Jung, Y. S. Nam, M. Jung, J. S. Park, S. Lee, H. Choi, S.-J. Ko, N. R. Shin, Y.-K. Kim, S. O. Kim, J. Y. Kim, H.-J. Shin, S. Cho, M. H. Song, *Adv. Mater.* **2014**, *26*, 494.
[43] A. Sreedharan, B. C. Das, *J. Phys. D: Appl. Phys.* **2022**, *55*, 335103.
[44] Y. Liu, L. Wang, B. Zhou, Y. Fu, D. Li, C. Guo, H. Wang, C. Chen, J. Cai, X. Zhang, W. Sun, D. Liu, W. Li, T. Wang, *ACS Materials Letters* **2022**, *5*, 321.
[45] A. F. Kohan, G. Ceder, D. Morgan, C. G. Van De Walle, *Phys. Rev. B* **2000**, *61*, 15019.
[46] X. Zhu, L. Hu, W. Wang, X. Jiang, L. Hu, Y. Zhou, *ACS Appl. Energy Mater.* **2019**, *2*, 7602.
[47] P. Jiang, L. Hu, L. Sun, Z. '. Li, H. Han, Y. Zhou, *Chem. Sci.* **2022**, *13*, 4714.

 © 2023 The Authors. Small Methods published by Wiley-VCH GmbH

23669608, 2024, 9, Downloaded from https://onlinelibrary.wiley.com/doi/10.1002/smtd.202301451 by Helmholtz-Zentrum Berlin Für, Wiley Online Library on [20/10/2025]. See the Terms and Conditions (https://onlinelibrary.wiley.com/terms-and-conditions) on Wiley Online Library for rules of use; OA articles are governed by the applicable Creative Commons License

[48] Z. Xu, M. M. Islam, R. Meitzner, A. Anand, A. S. Djoumessi, S. Stumpf, S. Hoeppener, C. Neumann, A. Turchanin, U. S. Schubert, H. Hoppe, *ACS Appl. Mater. Interfaces* **2023**, *15*, 45146.
[49] L. Hu, Y. Jiang, L. Sun, C. Xie, F. Qin, W. Wang, Y. Zhou, *Chem. Phys. Lett.* **2021**, *12*, 2607.
[50] J. Dagar, T. M. Brown, *Nanotechnology* **2022**, *33*, 405404.
[51] S. Yang, H. Yu, *Chem. Eng. J.* **2023**, *452*, 139658.
[52] S. K. Hau, H.-L. Yip, O. Acton, N. S. Baek, H. Ma, A. K.-Y. Jen, *J. Mater. Chem.* **2008**, *18*, 5113.
[53] Y. Lin, Y. Zhang, J. Zhang, M. Marcinskas, T. Malinauskas, A. Magomedov, M. I. Nugraha, D. Kaltsas, D. R. Naphade, G. T. Harrison, A. El-Labban, S. Barlow, S. De Wolf, E. Wang, I. Mcculloch, L. Tsetseris, V. Getautis, S. R. Marder, T. D. Anthopoulos, *Adv. Energy Mater.* **2022**, *12*, 2202503.
[54] Y. E. Ha, M. Y. Jo, J. Park, Y.-C. Kang, S. I. Yoo, J. H. Kim, *J. Phys. Chem. C* **2013**, *117*, 2646.
[55] H. Liu, Z.-X. Liu, S. Wang, J. Huang, H. Ju, Q. Chen, J. Yu, H. Chen, C.-Z. Li, *Adv. Energy Mater.* **2019**, *9*, 1900887.
[56] A. Tada, Y. Geng, M. Nakamura, Q. Wei, K. Hashimoto, K. Tajima, *Phys. Chem. Chem. Phys.* **2012**, *14*, 3713.
[57] J.-M. Chiu, C.-C. Chu, D. M. Zena, Y. Tai, *Appl. Energy* **2015**, *160*, 681.
[58] T. Zhu, J. Su, F. Labat, I. Ciofini, T. Pauporté, *ACS Appl. Mater. Interfaces* **2020**, *12*, 744.
[59] L. Huang, L. Chen, P. Huang, F. Wu, L. Tan, S. Xiao, W. Zhong, L. Sun, Y. Chen, *Adv. Mater.* **2016**, *28*, 4852.
[60] Y. Han, H. Dong, W. Pan, B. Liu, X. Chen, R. Huang, Z. Li, F. Li, Q. Luo, J. Zhang, Z. Wei, C.-Q. Ma, *ACS Appl. Mater. Interfaces* **2021**, *13*, 17869.
[61] C. E. Song, K. Y. Ryu, S.-J. Hong, C. Bathula, S. K. Lee, W. S. Shin, J.-C. Lee, S. K. Choi, J. H. Kim, S.-J. Moon, *ChemSusChem* **2013**, *6*, 1445.
[62] N. K. Elumalai, A. Uddin, *Energy Environ. Sci.* **2016**, *9*, 391.
[63] M. Xiong, J. Wu, Q. Fan, Q. Liu, J. Lv, X. Ou, X. Guo, M. Zhang, *Org. Electron.* **2021**, *96*, 106227.
[64] T. Chabbah, H. Abderrazak, P. Saint Martin, H. Casabianca, H. R. Kricheldorf, S. Chatti, *Polym. Adv. Technol.* **2020**, *31*, 2339.
[65] J. R. Lakowicz, *Principles of fluorescence spectroscopy*, Springer, New York City, **2006**.
[66] E. Pires, J. M. Fraile, *Phys. Chem. Chem. Phys.* **2020**, *22*, 24351.
[67] J. P. Guthrie, *Can. J. Chem.* **1978**, *56*, 2342.
[68] Z. Xu, J. P. Madalaimuthu, J. B. Slowik, R. Meitzner, A. Anand, S. Alam, H. Corte, S. Stumpf, U. S. Schubert, H. Hoppe, *Adv. Mater. Interfaces* **2023**, *10*, 2201740.
[69] Z. Xu, Q. Fan, X. Meng, X. Guo, W. Su, W. Ma, M. Zhang, Y. Li, *Chem. Mater.* **2017**, *29*, 4811.
[70] Q. Fan, Q. Zhu, Z. Xu, W. Su, J. Chen, J. Wu, X. Guo, W. Ma, M. Zhang, Y. Li, *Nano Energy* **2018**, *48*, 413.
[71] M. V. Khenkin, E. A. Katz, A. Abate, G. Bardizza, J. J. Berry, C. Brabec, F. Brunetti, V. Bulovic, Q. Burlingame, A. Di Carlo, R. Cheacharoen, Y.-B. Cheng, A. Colsmann, S. Cros, K. Domanski, M. Dusza, C. J. Fell, S. R. Forrest, Y. Galagan, D. Di Girolamo, M. Grätzel, A. Hagfeldt, E. Von Hauff, H. Hoppe, J. Kettle, H. Köbler, M. S. Leite, S. Liu, Y.-L. Loo, J. M. Luther, et al., *Nat. Energy* **2020**, *5*, 35.
[72] S. A. Paniagua, A. J. Giordano, O.' L. Smith, S. Barlow, H. Li, N. R. Armstrong, J. E. Pemberton, J.-L. Brédas, D. Ginger, S. R. Marder, *Chem. Rev.* **2016**, *116*, 7117.
[73] T. Lee, H. T. Bui, J. Yoo, M. Ra, S. H. Han, W. Kim, W. Kwon, *ACS Appl. Mater. Interfaces* **2019**, *11*, 41196.
[74] Y. Lin, Y. Zhang, A. Magomedov, E. Gkogkosi, J. Zhang, X. Zheng, A. El-Labban, S. Barlow, V. Getautis, E. Wang, L. Tsetseris, S. R. Marder, I. Mcculloch, T. D. Anthopoulos, *Mater. Horiz.* **2023**, *10*, 1292.
[75] I. Constantinou, N. T. Shewmon, C. K. Lo, J. J. Deininger, J. R. Reynolds, F. So, *Adv. Mater. Interfaces* **2016**, *3*, 1600741.
[76] Y.-M. Sung, Y.-C. Huang, F. S. Chien, C.-S. Tsao, *IEEE J. Photovolt.* **2019**, *9*, 694.
[77] H. Gu, L. Yan, S. Saxena, X. Shi, X. Zhang, Z. Li, Q. Luo, H. Zhou, Y. Yang, X. Liu, W. W. H. Wong, C.-Q. Ma, *ACS Appl. Energy Mater.* **2020**, *3*, 9714.

 © 2023 The Authors. Small Methods published by Wiley-VCH GmbH

23669608, 2024, 9, Downloaded from https://onlinelibrary.wiley.com/doi/10.1002/smtd.202301451 by Helmholtz-Zentrum Berlin Für, Wiley Online Library on [20/10/2025]. See the Terms and Conditions (https://onlinelibrary.wiley.com/terms-and-conditions) on Wiley Online Library for rules of use; OA articles are governed by the applicable Creative Commons License